communications physics

Article

https://doi.org/10.1038/s42005-024-01746-y

Manifestation of the quantum metric in chiral lattice systems

Francesco Di Colandrea [1], Nazanin Dehghan [1,2], Filippo Cardano [3], Alessio D'Errico [1,2] ✉ & Ebrahim Karimi [1,2]

Recent years have seen a surge in research on the role of quantum geometry in condensed matter physics. For instance, the Aharonov-Bohm effect is a physical phenomenon where the vector potential induces a phase shift of electron wavepackets in regions with zero magnetic fields due to an obstruction in space associated with a magnetic flux. A similar effect can be observed in solid-state systems, where the topology of the Berry connection can influence electron dynamics. These are paradigmatic examples of how the dynamics can be affected by the system's geometry. Here, we show that in chiral-symmetric processes the quantum metric has a measurable effect on the mean chiral displacement of delocalized wavefunctions. This finding is supported by a photonic experiment realizing a topological quantum walk and demonstrates an effect that can be attributed directly to the geometry of the state space.

Gauge fields play a fundamental role in modern physics. Besides being key mathematical objects for electromagnetism, quantum field theories, and electronic band structure, there has been a long debate on whether gauge fields should constitute the fundamental elements of the theory. In 1959, Y. Aharonov and D. Bohm[1] showed that electron wavefunctions can experience phase shifts induced by the vector potential even when crossing regions of space with zero electric or magnetic fields. This effect has been later verified in several experiments[2–9], and can be understood as a geometric-phase effect due to the presence of an obstruction in space[10–12]. Similar phenomena have been observed for water waves around flux vortices[13] and in optical systems[14,15]. The Aharonov-Bohm (AB) effect thus stimulated an ongoing debate on the physical nature of electromagnetic potentials[16–22].

The modern electronic band theory in solid-state physics predicts a plethora of phenomena associated with quantities analogous to the magnetic field and the vector potential in electromagnetism. These quantities are the Berry curvature $\mathbf{\Omega}$ and the Berry connection $\mathcal{A}$[11], respectively. The Berry curvature is a gauge-invariant field arising from the geometry of band eigenstates in the quasi-momentum space, which can introduce anomalous velocity effects to the motion of wavepackets when an external field is applied on the system[11,23–27]. The integral of the Berry curvature over the quasi-momentum space gives the topological invariant of Chern insulators[27–29]. This analogy can be exploited to design AB experiments in lattice systems, with the role of the vector potential played by the Berry connection. For instance, the AB effect has been observed in an atomic simulator of graphene, where $\mathbf{\Omega}$ is zero everywhere and singular in correspondence with the Dirac points[30]. Starting from the work of ref. 31, the Berry curvature has been revised as related to the imaginary part of a more general object, the quantum geometric tensor, whose real part provides a gauge-invariant metric in any submanifold of quantum states. This quantity is typically referred to as the quantum metric. The role of the quantum metric in quantum dynamics has sparked a strong interest in recent years[32–37].

In this work, we report the effect of the quantum metric on the motion of wavepackets. We focus on tight-binding models exhibiting chiral symmetry, and analyze the temporal evolution of wavepackets sharply peaked in the quasi-momentum space. Chiral symmetry is characterized by the existence of a unitary operator that pairs states with opposite energy (measured with respect to the Fermi level), and is typical of systems with two —or an even number of—sites per unit cell, such as models of polyacetylene chains[29,38] and graphene[39]. We evaluate the time evolution of the mean chiral displacement (MCD)[40–42], which gives the weighted difference in the mean position of the wavepacket distribution on the two sublattices. We show that, in the long-time limit, the MCD is directly related to the elements of the quantum metric. As a consequence of this result, the MCD can be used to measure the full quantum geometric tensor of chiral-symmetric systems.

This result is firstly verified with numerical simulations of different prototypical solid-state models, then experimentally observed in a photonic quantum walk where the lattice is encoded in the light transverse wavevector and the internal degree of freedom (sublattice) is associated with the optical polarization[27]. A chiral-symmetric unitary evolution operator is

[1]Nexus for Quantum Technologies, University of Ottawa, K1N 5N6 Ottawa, ON, Canada. [2]National Research Council of Canada, 100 Sussex Drive, Ottawa, ON, K1A 0R6, Canada. [3]Dipartimento di Fisica Ettore Pancini, Università degli Studi di Napoli Federico II, Complesso Universitario di Monte Sant'Angelo, via Cintia, 80126 Napoli, Italy. ✉e-mail: aderrico@uottawa.ca

implemented via patterned anisotropic devices. It is shown that the time-averaged MCD can be used to directly measure the quantum metric in one-dimensional (1D) topological quantum walks and extract the corresponding topological invariant.

Results

Theory

Consider a lattice system of arbitrary spatial dimension D formed by two sublattices, that is with two sites per unit cell. Precisely, the quantum states are elements of the Hilbert space $\mathcal{H}_\ell \otimes \mathcal{H}_s$, where $\mathcal{H}_\ell$ is spanned by eigenstates of the lattice position, and $\mathcal{H}_s$ is associated with a pseudo-spin degree of freedom, with $\dim(\mathcal{H}_s) = 2$.

Let us assume that the system possesses chiral symmetry, i.e., there exists a unitary operator $\hat{\Gamma}$, acting on $\mathcal{H}_s$, such that $\hat{\Gamma}\hat{U} = \hat{U}^{-1}\hat{\Gamma}$, where $\hat{U}$ is the unitary describing the single-particle evolution. In general, $\hat{\Gamma} = \mathbf{v}_\Gamma \cdot \hat{\boldsymbol{\sigma}}$, where the unit vector $\mathbf{v}_\Gamma$ identifies the eigenstates of the chiral operator on the Bloch sphere and $\hat{\boldsymbol{\sigma}} = (\sigma_x, \sigma_y, \sigma_z)$ is the vector of the three Pauli matrices. With an appropriate rotation in the pseudo-spin space, one can choose $\hat{\Gamma} = \hat{\sigma}_z := \mathrm{diag}[1, -1]$. Translation invariance and chiral symmetry allow us to write $\hat{U}$ in the block-diagonal form

$$\hat{U} = \int_{\mathrm{BZ}} \frac{d^D q}{(2\pi)^D}\, \mathcal{U}(\mathbf{q}) \otimes |\mathbf{q}\rangle\langle\mathbf{q}|, \tag{1}$$

where

$$\mathcal{U}(\mathbf{q}) = \exp(-iE(\mathbf{q})\, \mathbf{n}(\mathbf{q}) \cdot \hat{\boldsymbol{\sigma}}), \tag{2}$$

$$\mathbf{n}(\mathbf{q}) = (n_x(\mathbf{q}), n_y(\mathbf{q}), 0). \tag{3}$$

In Eqs. (1)-(2), $\mathbf{q}$ is the quasi-momentum, defined in the adimensional Brillouin Zone (BZ) –for square lattices, $\mathrm{BZ} = [-\pi, \pi]^{\otimes D}$–, $\mathcal{U}$ is an operator acting on $\mathcal{H}_s$, with eigenvalue E and eigenstate $\mathbf{n}$, with $|\mathbf{n}| = 1$. Equation (3) is a consequence of chiral symmetry: the eigenstates are represented on the Bloch sphere as unit vectors $\mathbf{n}(\mathbf{q})$, which lie in a plane perpendicular to the axis specified by the chiral operator (here chosen as the z-axis), i.e., $\mathbf{v}_\Gamma \cdot \mathbf{n}(\mathbf{q}) = 0$ for each $\mathbf{q}$. The manifold of the system's eigenstates, defined as $|\mathbf{n}(\mathbf{q})\rangle = (e^{-i\phi(\mathbf{q})}|\uparrow\rangle + |\downarrow\rangle)/\sqrt{2}$, with $\phi := \arctan(n_y/n_x)$ and $\hat{\Gamma} =: |\uparrow\rangle\langle\uparrow| - |\downarrow\rangle\langle\downarrow|$, can be equipped with a metric structure. Such quantum metric is derived from the quantum geometric tensor $\eta_{ij} = \langle\partial_i\psi|\partial_j\psi\rangle - \mathcal{A}_i\mathcal{A}_j$, where $\mathcal{A}_i = i\langle\psi|\partial_i\psi\rangle$ is the Berry connection. In our case, $|\psi\rangle \equiv |\mathbf{n}(\mathbf{q})\rangle$. The quantum metric thus provides a gauge-invariant geometric description of the state space. Indeed, the infinitesimal distance between two points in the state space (parametrized by $\mathbf{q}$) is given by $d\ell^2 = \mathrm{Re}[\eta_{ij}(\mathbf{q})]dq_i dq_j$[31]. In a chiral-symmetric system, the quantum geometric tensor is a real quantity and is given by

$$\eta_{ij}(\mathbf{q}) = \frac{1}{4}\partial_{q_i}\phi(\mathbf{q})\partial_{q_j}\phi(\mathbf{q}) =: \frac{1}{4}\gamma_i(\mathbf{q})\gamma_j(\mathbf{q}), \tag{4}$$

where $\gamma_i(\mathbf{q}) := (\mathbf{n}(\mathbf{q}) \times \partial_{q_i}\mathbf{n}(\mathbf{q})) \cdot \mathbf{v}_\Gamma$. The quantity $\gamma_i(\mathbf{q})$ has a simple geometrical interpretation, being proportional to the solid angle enclosed by the vectors $\mathbf{v}_\Gamma$, $\mathbf{n}(\mathbf{q})$, and $\mathbf{n}(\mathbf{q} + d\mathbf{q})$ in the unit sphere[43]. Note that, within our gauge choice, $\gamma_i(\mathbf{q}) = 2\mathcal{A}_i(\mathbf{q})$.

In 1D lattices, chiral symmetry allows defining a topological invariant, the winding number ν, associated with the number of times the vector $\mathbf{n}(\mathbf{q})$ spans the plane when the quasi-momentum runs across one BZ. It has been proven that the MCD provides an observable quantity tracking the topological invariant of 1D chiral systems[40–42,44–46]. Here, we show that the MCD can also be employed to probe the quantum metric.

For two-band models, the MCD is defined as

$$\mathcal{C}_i(t) = 2\langle\psi(t)|\hat{\Gamma}\hat{x}_i|\psi(t)\rangle, \tag{5}$$

where $\hat{x}_i$ is the i-th component of the lattice position operator and $|\psi(t)\rangle = \hat{U}^t|\psi(0)\rangle$, $|\psi(0)\rangle$ being the system wavefunction at time $t = 0$. Equation (5) can be interpreted as the weighted difference between the mean positions on the two sublattices (where the weights are given by the probability of being in either sublattice). The MCD asymptotically converges to the winding number if $|\psi(0)\rangle$ is either a localized state[40] or, more generally, if it can be mapped to a localized state via a translation-invariant unitary operator[42].

In this work, a different scenario is considered, where the initial state is a wavepacket exhibiting a narrow distribution in the reciprocal lattice, $|\psi(0)\rangle = \int_{\mathrm{BZ}} d^D q/(2\pi)^D\, G_{w,\mathbf{q}_0}(\mathbf{q})|\mathbf{q}\rangle \otimes |\phi_0\rangle$, where $|\phi_0\rangle$ is a sublattice state and $G_{w,\mathbf{q}_0}(\mathbf{q})$ a function peaked around $\mathbf{q}_0$ with characteristic width w. We obtain—see Methods "Proof of the main result" for the detailed derivation–

$$\begin{aligned}\mathcal{C}_i(t) &= 2\int_{\mathrm{BZ}} \frac{d^D q}{(2\pi)^D}|G_{w,\mathbf{q}_0}|^2 \sin^2(tE)\gamma_i \\ &= \int_{\mathrm{BZ}} \frac{d^D q}{(2\pi)^D}|G_{w,\mathbf{q}_0}|^2 \gamma_i(1 - \cos(2Et)).\end{aligned} \tag{6}$$

The last integral in Eq. (6) gives an oscillating contribution that generally decreases in amplitude as $\sim 1/\sqrt{t}$, and thus, asymptotically, we obtain

$$\mathcal{C}_i \sim \int_{\mathrm{BZ}} \frac{d^D q}{(2\pi)^D}\, |G_{w,\mathbf{q}_0}(\mathbf{q})|^2 \gamma_i(\mathbf{q}). \tag{7}$$

For initial states narrowly peaked in the reciprocal lattice ($w \to 0$), the MCD can thus probe the local value of γ_i:

$$\mathcal{C}_i \sim \gamma_i(\mathbf{q}_0). \tag{8}$$

If $|G_{w,\mathbf{q}_0}|^2 = g_w(\mathbf{q} - \mathbf{q}_0)$, Equation (6) can be seen as the convolution between the function g_w and $\sin^2(tE)\gamma_i$. Hence, one can extract $\sin^2(tE)\gamma_i$ for finite widths w via a deconvolution analysis of the measured $\mathcal{C}_i$ as a function of $\mathbf{q}_0$. The factor $\sin^2(tE)$ is either $\mathbf{q}$–independent—in the case of flat bands—or averages to 1/2 in the long-time limit. The quantum metric can thus be extracted also in situations with evolutions limited in time by evaluating the time average of the deconvolved MCD. For chiral-symmetric systems, the quantum geometric tensor can be effectively reconstructed as

$$\eta_{ij} = \frac{1}{4}\tilde{\mathcal{C}}_i\tilde{\mathcal{C}}_j, \tag{9}$$

where $\tilde{\mathcal{C}}_i$ is the time-averaged MCD along x_i.

We note that the MCD carries a sign ambiguity since the same system is symmetric under the action of both $\hat{\Gamma}$ and $-\hat{\Gamma}$. However, this does not affect the sign of the quantum geometric tensor components.

A comparison between the time-averaged MCD of two typical chiral models is shown in Fig. 1 (see Methods "Details on numerical simulations" for more details). In both cases, the initial state is a Gaussian wavepacket sharply peaked around a given quasi-momentum value $\mathbf{q}_0$, $G_{w,\mathbf{q}_0} = \mathcal{N}\exp(-(\mathbf{q} - \mathbf{q}_0)^2/w^2)$, where $\mathcal{N}$ is a normalization factor. In panels a and b, the Su-Schrieffer-Heeger (SSH) model for a composite 1D lattice is considered[38]. The parameters a and b correspond to the intracell and intercell hopping amplitudes, respectively. The MCD is evaluated for different values of q_0 spanning the BZ. The agreement between $\tilde{\mathcal{C}}$ and the quantity γ is evident after $t = 30/a$. In Fig. 1c, d, the same simulation is performed for the two-band tight-binding graphene. The time-averaged MCD converges to $\boldsymbol{\gamma}$. Although not evident in the figure, this convergence fails in the extreme vicinity of the Dirac points, where $\boldsymbol{\gamma}$ diverges and the MCD falls to zero. As shown in Methods "Details on numerical simulations", this is due to the $\sin(Et)^2$ factor rapidly falling to zero.

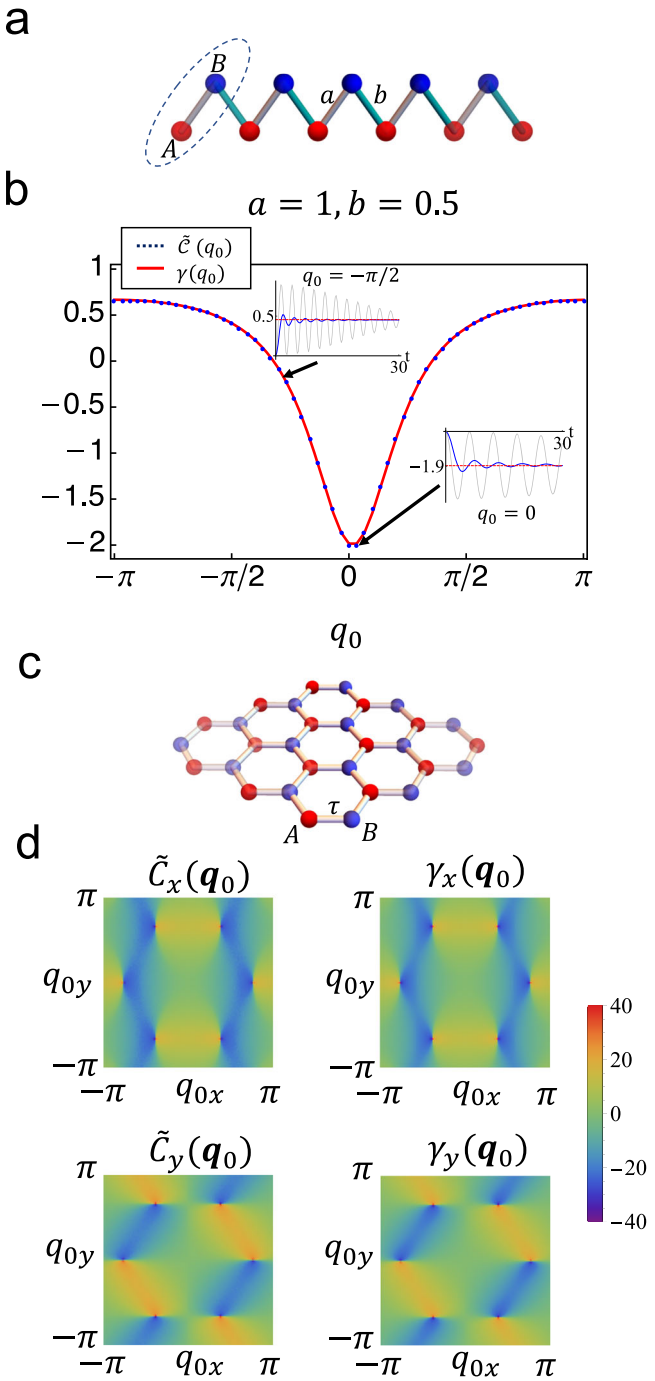

Fig. 1 | Mean chiral displacement (MCD) and quantum metric in chiral models. **a** Schematics of the Su-Schrieffer-Heeger (SSH) model. **b** Time-averaged MCD for the SSH model, evaluated for wavepackets ($w = 0.1$) centered in different points of the Brillouin zone (blue points), and compared with the square root of the quantum metric (red curve) after $t = 30/a$. Insets show the dynamical evolution of the MCD (gray lines), and its average in time (blue line), for selected quasi-momentum values. **c** Schematics of two-band graphene model. **d** Comparison of time-averaged MCD ($50/\tau \leq t \leq 60/\tau$, where τ is the hopping amplitude between the two sublattices, $w = \pi/10$) and γ in two-band graphene. Note that the color scale is truncated to the maximum of the MCD since γ diverges in the proximity of the Dirac cones.

Experimental results

The effect of the quantum metric on the MCD of wavepackets is experimentally investigated in a photonic quantum walk (QW). In this experiment, the sublattice degree of freedom is encoded into the polarization of light. The lattice can be encoded in an infinite-dimensional degree of freedom, such as the (discretized) transverse wavevector[27,47,48]. Each lattice site thus corresponds to an optical mode which can be approximated as a plane wave with a slightly tilted wavefront. In other words, a position x on the lattice maps into a transverse wavevector equal to $k = 2\pi x/\Lambda$—where Λ is a constant related to the inverse of the lattice spacing. Following the approach recently devised in ref. 49, the chiral-symmetric unitary is implemented by a minimal stack of three patterned waveplates, specifically a half-wave plate sandwiched between two quarter-waveplates. This scheme allows realizing a space-dependent polarization transformation which maps into the target evolution[49].

The chiral process considered here is the QW introduced in ref. 40. The unit step $U = T \cdot W$ consists of a polarization rotation $W := (\sigma_0 + i\sigma_x)/\sqrt{2}$, followed by a polarization-dependent lattice translation $T := \sum_x (|x+1\rangle\langle x| \otimes \sigma_- + |x-1\rangle\langle x| \otimes \sigma_+)$, where $\sigma_\pm = \sigma_x \mp i\sigma_y$. Here, it is assumed that the positive and negative eigenstates of σ_z are left and right circular polarizations, $|L\rangle$ and $|R\rangle$, respectively. While long evolutions are typically achieved by stacking single-step waveplates[40,42,47], here, the more compact approach of designing only three plates implementing either $t = 10$ or $t = 11$ steps is adopted. For our protocol, it is sufficient to consider the average of $2n$-step and $(2n+1)$-step processes (with n an integer number), e.g., U^{10} and U^{11}, to observe adequate convergence of the time-averaged MCD to the local quantum metric. This choice is justified by the fact that the energy band dispersion allows for a suitable wavepacket width such that the oscillating terms in Eq. (6) feature opposite contributions, almost canceling each other when taking the average $\tilde{\mathcal{C}} = (\mathcal{C}(t = 2n) + \mathcal{C}(t = 2n+1))/2$. A rigorous proof is provided in Methods "Oscillating terms for the QW protocol" via asymptotic estimates, also confirmed by numerical simulations.

A simplified experimental setup is shown in Fig. 2a (see Methods "Details on the experimental setup" for more details). A collimated laser beam ($\lambda = 810$ nm) is prepared in an arbitrary polarization state and propagates through three patterned waveplates implementing U^t. A projection is then performed onto the two eigenstates of the chiral operator:

$$|\uparrow\rangle = \cos\left(\frac{\pi}{8}\right)|L\rangle - i\sin\left(\frac{\pi}{8}\right)|R\rangle, \tag{10}$$

$$|\downarrow\rangle = \sin\left(\frac{\pi}{8}\right)|L\rangle + i\cos\left(\frac{\pi}{8}\right)|R\rangle. \tag{11}$$

The lattice space, being associated with the transverse wavevector of the light beam, is accessed via an optical Fourier transform, i.e., by measuring the intensity distribution $I_{\uparrow/\downarrow}(x)$ in the focal plane of a lens placed after the polarization projection stage. The MCD is experimentally retrieved by measuring the weighted difference between the center of mass of the intensity distributions of the two chiral projections: $\mathcal{C} = 2\sum_x (I_\uparrow(x) - I_\downarrow(x))x$, where it is assumed that the intensities are normalized according to $\sum_x (I_\uparrow(x) + I_\downarrow(x)) = 1$. Here, with a slight abuse of notation, we identify the coordinate x at the lens focus with the index specifying the correct mapping. This identification is obtained by expressing x in units of the lattice spacing. The latter depends on the inverse of the characteristic period $\Lambda = 0.25$ cm of the plates implementing the QW evolution and the focal length $f = 25$ cm of the lens implementing the Fourier transform. The distance Λ also corresponds to the physical extension of a single BZ in our setup[27]. In this implementation, the lattice sites are mapped into states carrying x units of transverse momentum $2\pi/\Lambda$, and as a consequence, the quasi-momentum q corresponds to the transverse position X in the region of space where the waveplates are positioned—see Methods "Relationship between experimental and simulated coordinate spaces" and ref. 27 for more details. The plates implementing the QW are liquid-crystal metasurfaces exhibiting a position-dependent optic-axis orientation $\theta(X)$, plotted in Fig. 2b. The optical retardation δ of these devices is uniform but can be tuned. The first and last plates, L_1 and L_3, act as quarter-wave plates, $\delta_{1,3} = \pi/2$, while the intermediate plate, L_2, acts as a half-wave plate, $\delta_2 = \pi$. In this setup, the width w of the initial wavefunction in the reciprocal lattice is proportional to the laser beam waist w_0 (measured on the patterned waveplates' plane). With a large waist, $w_0 \geq \Lambda$, we measure a global MCD,

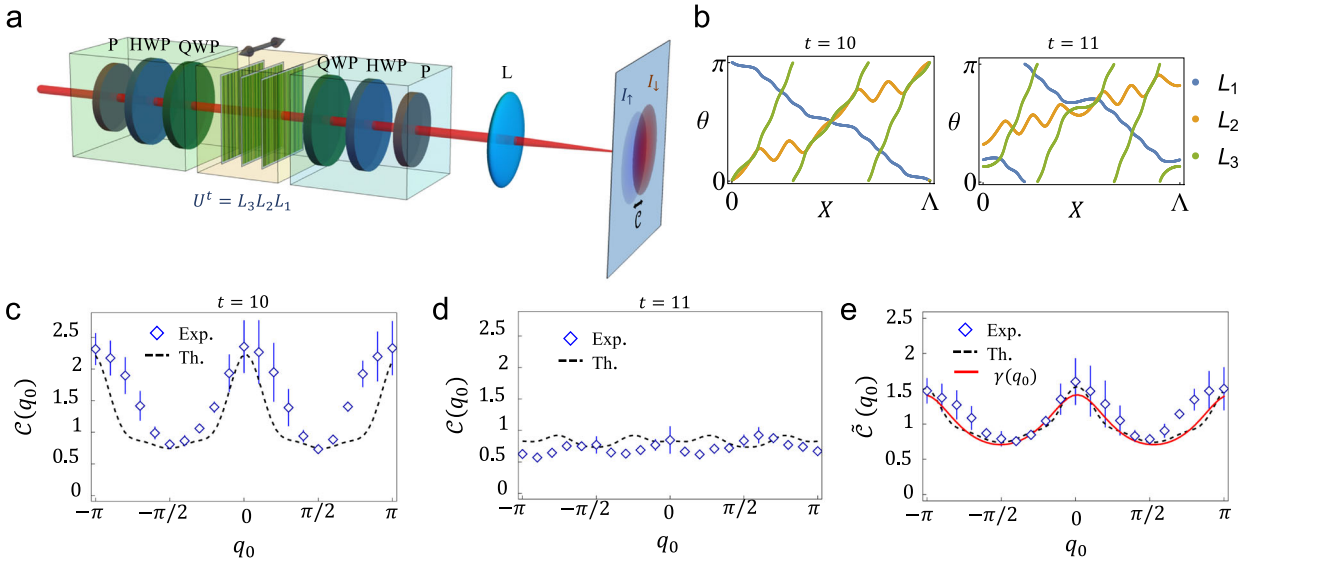

Fig. 2 | MCD induced by the quantum metric in a photonic quantum walk. **a** Sketch of the experimental setup. The laser beam is prepared in an arbitrary polarization state, set by a polarizer (P), a half-wave plate (HWP), and a quarter-wave plate (QWP). To simulate wavepacket dynamics, the beam waist is adjusted so as $w_0 < \Lambda$. The overall chiral-symmetric evolution operator, U^t, is implemented via three liquid-crystal metasurfaces. A rigid translation of the bulk of plates along the X direction is equivalent to changing the value q_0 for the wavepacket. After the QW, a projection onto the chiral eigenstates, $|\uparrow\rangle$ and $|\downarrow\rangle$, is performed, and the resulting intensity is recorded in the focal plane of a lens (L), corresponding to the lattice space of the QW. The difference in the centroid position of the two intensity distributions, $I_\uparrow$ and $I_\downarrow$, gives the mean chiral displacement (MCD). **b** Optic-axis patterns $\theta(X)$ of the liquid-crystal plates $L_{1,2,3}$ implementing $t = 10$ and $t = 11$ steps. The distance $\Lambda = 0.25$ cm corresponds to the largest spatial period and defines a BZ. The lattice spacing in the transverse-wavevector domain is thus $2\pi/\Lambda$. **c**, **d** The measured MCD at $t = 10$ and $t = 11$ is compared with theoretical predictions. **e** The time-averaged MCD obtained experimentally is compared with the average computed from a complete simulation of the ideal QW evolution (dashed curve) and with the quantity γ, proportional to the square root of the quantum metric (red curve). **c**–**e** Error bars are standard deviations over four repeated measurements. Where the bar is not visible, it is smaller than the data point.

which asymptotically yields the topological invariant $\nu = 1$ associated with the chosen QW[40]. For $w_0 < \Lambda$, we can locally sample the BZ. We used $w_0 \sim 0.13\,\Lambda$. The value of q_0 is simply changed by translating the three metasurfaces in the X direction, thus introducing an effective transverse displacement with respect to the beam propagation. The reciprocal lattice is sampled in steps of $\Delta X = 0.12$ mm, for a total of $n = \Lambda/\Delta X = 21$ points. Figure 2c, d show the measured MCD for $t = 10$ and $t = 11$ steps, respectively, compared with theoretical curves evaluated from Eq. (6). Errors are reported as the standard deviations over four repeated measurements. In Fig. 2e, the square root of the metric is compared with the average $\tilde{\mathcal{C}}(q_0) := (\mathcal{C}(q_0, t = 10) + \mathcal{C}(q_0, t = 11))/2$. We observe a good agreement with the theory. Some deviations can be ascribed to imperfections in the fabrication process and relative misalignment of the plates. Note that the measured $\tilde{\mathcal{C}}(q_0)$, when integrated over the BZ, yields $\nu = 1.15 \pm 0.19$, fully compatible with the expected value of the topological invariant and with the experimental value measured for initial localized states (see Methods "Experimental results for localized input states").

Conclusion

It has been shown that the quantum metric affects the relative spatial distribution of wavepackets on the two sublattices of chiral-symmetric systems. This effect is captured by the MCD. This result has been verified numerically on solid-state models, specifically the SSH model and graphene, and experimentally in a 1D photonic quantum walk. In analogy with the AB effect, the MCD can be non-zero in regions where the Berry curvature vanishes. In the particular case of 1D systems, where the Berry curvature is not defined, this effect is still observed and proportional to the square root of the quantum metric. Our work offers a method to measure the quantum metric of unitary processes on lattice systems, from which geometrical and topological features can be extracted. Future developments will concern the generalization of this result to higher-dimensional sublattices, which will allow developing investigation methods for chiral-symmetric two and three-dimensional topological insulators.

Methods

Proof of the main result

From Eq. (5), using Eq. (1) and the momentum representation of the position operator, $\langle \mathbf{q}|\hat{x}_i|\mathbf{q}'\rangle = i\delta(\mathbf{q}-\mathbf{q}')\partial_{q_i}$, we obtain

$$\begin{aligned}\mathcal{C}_i(t) = 2i\int_{\mathrm{BZ}} \frac{d^D q}{(2\pi)^D} |G_{w,\mathbf{q}_0}|^2 \langle \phi_0|\mathcal{U}^{-t}\hat{\Gamma}\partial_{q_i}\mathcal{U}^t|\phi_0\rangle \\ + 2i\int_{\mathrm{BZ}} \frac{d^D q}{(2\pi)^D} \langle \phi_0|\mathcal{U}^{-t}\hat{\Gamma}\mathcal{U}^t|\phi_0\rangle \frac{\partial_{q_i}|G_{w,\mathbf{q}_0}|^2}{2},\end{aligned} \tag{12}$$

where we suppressed the dependency on the quasi-momentum to simplify the notation. Using $\mathcal{U}^t = \cos(Et)\sigma_0 - i\sin(Et)\mathbf{n}\cdot\hat{\boldsymbol{\sigma}}$, where σ_0 is the identity operator, and $\mathcal{U}^{-t}\Gamma = \Gamma\mathcal{U}^t$, we obtain

$$\begin{aligned}\mathcal{U}^{-t}\hat{\Gamma}\partial_{q_i}\mathcal{U}^t &= \frac{1}{2}\hat{\Gamma}\partial_{q_i}(\cos(2tE) - i\sin(2tE)\mathbf{n}\cdot\hat{\boldsymbol{\sigma}}) \\ &\quad - i\sin^2(tE)(\mathbf{n}\times\partial_{q_i}\mathbf{n})\cdot\mathbf{v}_\Gamma \\ &= \frac{1}{2}\hat{\Gamma}\partial_{q_i}\mathcal{U}^{2t} - i\sin^2(tE)\gamma_i.\end{aligned} \tag{13}$$

In the last equality, we used $\gamma_i = (\mathbf{n}\times\partial_{q_i}\mathbf{n})\cdot\mathbf{v}_\Gamma$. Thus,

$$\begin{aligned}\mathcal{C}_i(t) = 2\int_{\mathrm{BZ}} \frac{d^D q}{(2\pi)^D} |G_{w,\mathbf{q}_0}|^2 \sin^2(tE)\gamma_i \\ + 2i\int_{\mathrm{BZ}} \frac{d^D q}{(2\pi)^D} |G_{w,\mathbf{q}_0}|^2 \frac{1}{2}\langle \phi_0|\hat{\Gamma}\partial_{q_i}\mathcal{U}^{2t}|\phi_0\rangle \\ + 2i\int_{\mathrm{BZ}} \frac{d^D q}{(2\pi)^D} \langle \phi_0|\hat{\Gamma}\mathcal{U}^{2t}|\phi_0\rangle \frac{\partial_{q_i}|G_{w,\mathbf{q}_0}|^2}{2}.\end{aligned} \tag{14}$$

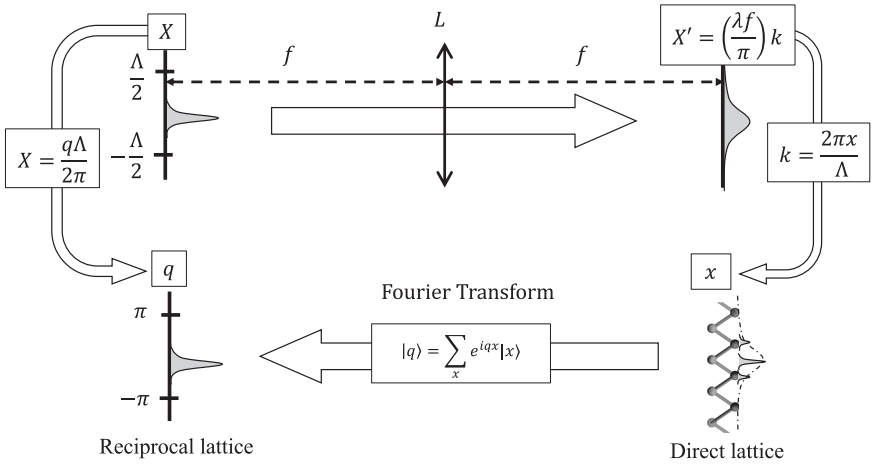

Fig. 3 | Experimental encoding of the model parameters. The transverse coordinate X in the plane of the metasurfaces is mapped into the reciprocal lattice coordinate q, and the characteristic distance Λ corresponds to one Brillouin Zone. A narrow wavepacket in the reciprocal lattice thus corresponds to a beam crossing the X plane with waist parameter $w_0 \ll \Lambda$. The transverse coordinate X' in the focal plane of the Fourier-transforming lens (L) is mapped in the lattice position x of the QW via the relation $X' = 2\lambda f x/\Lambda$. Note that x and q are considered adimensional quantities.

Integration by parts shows that the last two terms cancel each other:

$$\begin{aligned}\mathcal{C}_i(t) &= 2\int_{\mathrm{BZ}} \frac{d^D q}{(2\pi)^D} |G_{w,\mathbf{q}_0}|^2 \sin^2(tE)\gamma_i \\ &= \int_{\mathrm{BZ}} \frac{d^D q}{(2\pi)^D} |G_{w,\mathbf{q}_0}|^2 \gamma_i \\ &\quad - \int_{\mathrm{BZ}} \frac{d^D q}{(2\pi)^D} |G_{w,\mathbf{q}_0}|^2 \cos(2Et)\gamma_i.\end{aligned} \tag{15}$$

Using the stationary phase approximation, it can be shown that the last integral gives a contribution that oscillates in time and generally decreases in amplitude as $\sim 1/\sqrt{t}$, from which the final result of Eq. (7) is derived. Note that, in the case of flat bands $E(\mathbf{q})$ = constant, the asymptotic result is exact apart from a $\sin^2(tE)$ multiplicative factor.

As discussed in the main text, if $|G_{w,\mathbf{q}_0}|^2 = g_w(\mathbf{q} - \mathbf{q}_0)$, the quantum metric can be extracted from the time average of the deconvolved MCD.

Details on numerical simulations

SSH Hamiltonian. The SSH model[38] describes a composite 1D lattice with two sites per unit cell. The lattice Hamiltonian is

$$H = \sum_x a|x, B\rangle\langle x, A| + b|x+1, A\rangle\langle x, B| + \text{ h.c.}\,, \tag{16}$$

where $x \in \mathbb{Z}$ labels the lattice sites, the two sublattices are labeled as A and B, and h.c. denotes the Hermitian conjugate. The coefficients a and b are the intracell and intercell hopping amplitudes, respectively. The Bloch theorem allows diagonalizing H as $H = \int (dq/2\pi)\,\mathcal{H}(q) \otimes |q\rangle\langle q|$, with $\mathcal{H}(q) = E(q)\mathbf{n}(q)\cdot\hat{\boldsymbol{\sigma}}$, where

$$\begin{aligned}E(q) &= \sqrt{a^2 + 2ab\cos(q) + b^2}, \\ n_x(q) &= \frac{a + b\cos(q)}{E(q)}, \\ n_y(q) &= \frac{b\sin(q)}{E(q)}, \\ n_z(q) &= 0.\end{aligned} \tag{17}$$

The chiral operator is $\Gamma = \sigma_z$.

Graphene Hamiltonian. A simple nearest-neighbor tight-binding model for graphene, which only includes the two energy bands near the Fermi energy, gives the following Bloch Hamiltonian $\mathcal{H}$[39]:

$$\begin{aligned}\mathcal{H}(q_x, q_y) = &-\tau\sigma_x\left[\cos\left(\frac{\sqrt{3}q_y}{2} - \frac{q_x}{2}\right)\right. \\ &\left. + \cos\left(\frac{q_x}{2} + \frac{\sqrt{3}q_y}{2}\right) + \cos(q_x)\right] \\ &+ \tau\sigma_2\left[\sin\left(\frac{\sqrt{3}q_y}{2} - \frac{q_x}{2}\right)\right. \\ &\left. - \sin\left(\frac{q_x}{2} + \frac{\sqrt{3}q_y}{2}\right) + \sin(q_x)\right],\end{aligned} \tag{18}$$

where τ denotes the hopping amplitude. The energy bands of graphene display Dirac cones in the points $\mathbf{K} = (2\pi/3, 2\pi/3\sqrt{3})$ and $\mathbf{K}' = (2\pi/3, -2\pi/3\sqrt{3})$ of the BZ. In the proximity of these points, the Hamiltonian takes the form $\mathcal{H}(\mathbf{k}) = v_{\mathrm{F}}\mathbf{k}\cdot\boldsymbol{\sigma}$, where $\mathbf{k} = \mathbf{q} - \mathbf{K}$ and $v_{\mathrm{F}} = 3\tau/2$. Straightforward calculations show that $\boldsymbol{\gamma}(k_x, k_y) = 2(-k_y, k_x)/(k_x^2 + k_y^2)$, which diverges in $\mathbf{k} = 0$. However, the MCD is also affected by the $\sin^2(tE)$ factor, which approximates to $\sin^2(tE) \sim 9|\mathbf{k}|^2 t^2/4$ in the vicinity of the cone. The MCD is thus given by

$$\mathcal{C}(\mathbf{k}, t) = 9t^2 \int_{BZ} |G_{w,\mathbf{k}_0}(\mathbf{k})|^2 (-k_y, k_x)\frac{dk_x, dk_y}{4\pi^2}, \tag{19}$$

which goes to zero for $\mathbf{q} \to \mathbf{K}$ (and similarly for $\mathbf{K}'$).

Oscillating terms for the QW protocol

In this section, we analyze the behavior of the oscillating contributions in the MCD for our QW protocol $\hat{U} = \hat{T}\hat{W}$. As evident from the results presented in the main text, for a fixed number of time steps, the strongest deviations of the MCD from the quantum metric appear around $q = 0$ and $q = \pi$. These are critical points for the energy $E(q)$. The integral to be evaluated is

$$\begin{aligned}I_{q_0}(t) &:= \int \frac{dq}{2\pi} g_w(q - q_0)\gamma_i(q)\cos(2Et) \\ &= \mathrm{Re}\int \frac{dq}{2\pi} g_w(q - q_0)\gamma_i(q)\exp(i2Et).\end{aligned} \tag{20}$$

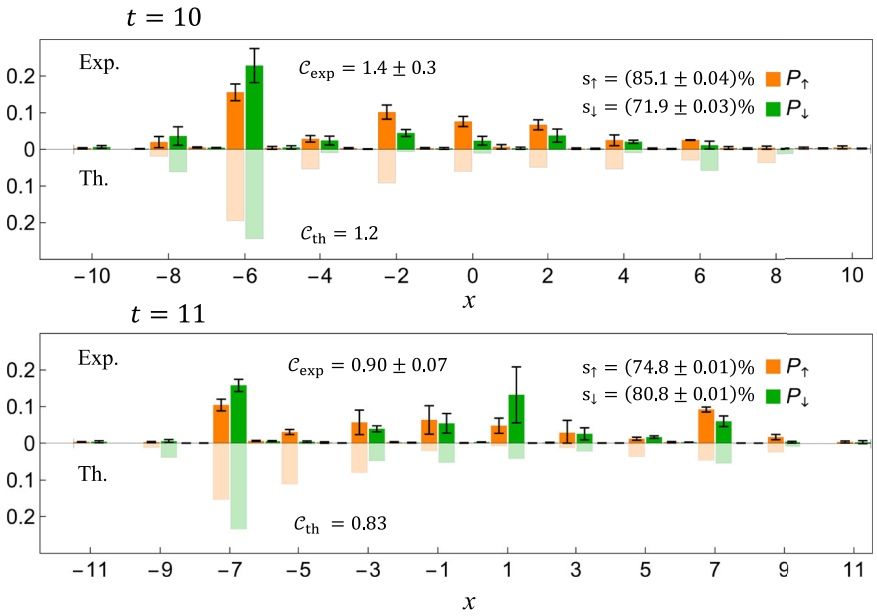

Fig. 4 | Probability distributions for localized inputs. Comparison between experimental and theoretical probability distributions after $t = 10$ and $t = 11$ steps for a $|L\rangle$-polarized localized initial state ($w_0 > \Lambda$), obtained after projecting on the chiral eigenstates $|\uparrow\rangle$ ($P_\uparrow$) and $|\downarrow\rangle$ ($P_\downarrow$). The experimentally measured MCD $\mathcal{C}_{exp}$, the theoretical prediction $\mathcal{C}_{th}$, and the similarity between the distributions are provided. Errors are reported as the standard deviations over four repeated measurements.

For large t, the last expression can be estimated via the stationary phase approximation:

$$\begin{aligned}&\mathrm{Re}\int\frac{dq}{2\pi}g_w(q-q_0)\gamma_i(q)\exp(i2Et)\\&\sim\sqrt{\frac{1}{2\pi t}}\,\mathrm{Re}\left[\frac{e^{i\pi/4}}{\sqrt{2|E''(\pi)|}}\gamma_i(\pi)g_w(\pi-q_0)e^{i2tE(\pi)}\right.\\&\left.+\frac{e^{-i\pi/4}}{\sqrt{2|E''(0)|}}\gamma_i(0)g_w(-q_0)e^{i2tE(0)}\right],\end{aligned}\tag{21}$$

where $E''(q^*) := d^2E/dq^2|_{q=q^*}$. If $g_w(q)$ is a narrow function centered in $q = 0$, the contribution from $I_{q_0}(t)$ is not negligible for $q_0 \approx \pi$ and $q_0 \approx 0$. Say $q_0 \approx \pi$ (the same analysis holds for $q_0 \approx 0$), then the oscillating contribution is proportional to $\cos(2E(\pi)t + \pi/4)/\sqrt{t}$. For our protocol, $E(\pi) = \pi/4$ (while $E(0) = 3\pi/4$), thus $I_\pi(t) \propto \cos(\pi t/2 + \pi/4)/\sqrt{t}$. For successive t, with $t_1 = 2n$ and $t_2 = 2n + 1$, with n an integer number, this function flips sign and its amplitude decreases as $\sqrt{t/(t+1)}$, which can be approximated with 1 for large t. Thus, averaging the MCD over two successive steps, provided that the first time step is an even number, dramatically reduces the oscillating contributions. It must be noted that a finite width of the wavepacket is necessary for this argument to hold. If the wavepacket is extremely narrow in the BZ, then $\mathcal{C} \approx \gamma_i(q_0)(1 - \cos(2E(q_0)t))$ and a multi-step average is generally necessary.

Details on the experimental setup

The laser source is the output of a Titanium-Sapphire (Ti:Sa) laser (central wavelength 810 nm, pulse duration 150 fs, repetition rate 40 MHz), spatially cleaned through a single-mode fiber. The beam waist is $w_0 \simeq 2.5$ mm to simulate localized initial states, and $w_0 \simeq 0.32$ mm for wavepacket dynamics.

The liquid-crystal metasurfaces implementing the unitary evolution are fabricated with a photoalignment technique, based on orienting a dye solution (PAAD-22), spin-coated on ITO glasses, with linearly polarized light at 405 nm. The liquid crystal (6CHBT) is inserted in the sample via capillarity and locally aligns with the dye. Electrical contacts applied on the edges of the ITO surfaces allow tuning the optical retardation of the devices to the desired value. An alternate voltage with a sinusoidal wave at 10 kHz is used in the experiment.

Relationship between experimental and simulated coordinate spaces

The walker lattice space is encoded in the transverse-wavevector space of the light beam crossing the patterned waveplates. As illustrated in Fig. 3, this means that the transverse position X (modulo Λ) in the plane of the liquid-crystal metasurfaces corresponds to the quasi-momentum q, while the far-field corresponds to the lattice space. Accordingly, a wavepacket corresponds to a beam having waist $w_0 < \Lambda$ in the X plane. The value q_0 can be controlled either by laterally shifting the wavepacket or, more practically, by translating the metasurfaces along the X direction. The proper conversion factors from the setup to the model parameters are provided in Fig. 3.

Experimental results for localized input states

We measure the QW distributions for localized input states after $t = 10$ and $t = 11$ time steps. The results are shown in Fig. 4. The agreement between the experimental observation and the theoretical prediction is quantified in terms of the similarity, $s = (\sum_x \sqrt{P_{exp}(x)P_{th}(x)})^2$, where P_{exp} and P_{th} are the normalized experimental and theoretical probability distributions, respectively.

Data availability

The data were available from the corresponding author upon reasonable request.

Code availability

The code used for the data analysis is available from the corresponding author upon reasonable request.

Received: 28 February 2024; Accepted: 14 July 2024;
Published online: 05 August 2024

References

1. Aharonov, Y. & Bohm, D. Significance of electromagnetic potentials in the quantum theory. *Phys. Rev.* **115**, 485–491 (1959).
2. Tonomura, A. et al. Observation of Aharonov-Bohm effect by electron holography. *Phys. Rev. Lett.* **48**, 1443–1446 (1982).
3. Webb, R. A., Washburn, S., Umbach, C. P. & Laibowitz, R. B. Observation of $\frac{h}{e}$ Aharonov-Bohm oscillations in normal-metal rings. *Phys. Rev. Lett.* **54**, 2696–2699 (1985).

4. Matteucci, G. & Pozzi, G. New diffraction experiment on the electrostatic Aharonov-Bohm effect. *Phys. Rev. Lett.* **54**, 2469–2472 (1985).
5. Tonomura, A. et al. Evidence for aharonov-bohm effect with magnetic field completely shielded from electron wave. *Phys. Rev. Lett.* **56**, 792–795 (1986).
6. Timp, G. et al. Observation of the Aharonov-Bohm effect for $\omega_c\tau>1$. *Phys. Rev. Lett.* **58**, 2814–2817 (1987).
7. Allman, B. E. et al. Scalar Aharonov-Bohm experiment with neutrons. *Phys. Rev. Lett.* **68**, 2409–2412 (1992).
8. Bachtold, A. et al. Aharonov–Bohm oscillations in carbon nanotubes. *Nature* **397**, 673–675 (1999).
9. Haug, T., Heimonen, H., Dumke, R., Kwek, L.-C. & Amico, L. Aharonov-Bohm effect in mesoscopic bose-einstein condensates. *Phys. Rev. A* **100**, 041601 (2019).
10. Yau, J.-B., De Poortere, E. P. & Shayegan, M. Aharonov-Bohm oscillations with spin: evidence for berry's phase. *Phys. Rev. Lett.* **88**, 146801 (2002).
11. Xiao, D., Chang, M.-C. & Niu, Q. Berry phase effects on electronic properties. *Rev. Mod. Phys.* **82**, 1959–2007 (2010).
12. Cohen, E. et al. Geometric phase from Aharonov–Bohm to Pancharatnam–Berry and beyond. *Nat. Rev. Phys.* **1**, 437–449 (2019).
13. Berry, M., Chambers, R., Large, M., Upstill, C. & Walmsley, J. Wavefront dislocations in the Aharonov-Bohm effect and its water wave analogue. *Eur. J. Phys.* **1**, 154 (1980).
14. Li, E., Eggleton, B. J., Fang, K. & Fan, S. Photonic Aharonov–Bohm effect in photon–phonon interactions. *Nat. Commun.* **5**, 3225 (2014).
15. Parto, M. et al. Observation of twist-induced geometric phases and inhibition of optical tunneling via Aharonov-Bohm effects. *Sci. Adv.* **5**, eaau8135 (2019).
16. DeWitt, B. S. Quantum theory without electromagnetic potentials. *Phys. Rev.* **125**, 2189–2191 (1962).
17. Vaidman, L. Role of potentials in the Aharonov-Bohm effect. *Phys. Rev. A* **86**, 040101 (2012).
18. Aharonov, Y., Cohen, E. & Rohrlich, D. Comment on "role of potentials in the aharonov-bohm effect". *Phys. Rev. A* **92**, 026101 (2015).
19. Vaidman, L. Reply to "comment on role of potentials in the Aharonov-Bohm effect". *Phys. Rev. A* **92**, 026102 (2015).
20. Aharonov, Y., Cohen, E. & Rohrlich, D. Nonlocality of the aharonov-bohm effect. *Phys. Rev. A* **93**, 042110 (2016).
21. Li, X., Hansson, T. H. & Ku, W. Gauge-independent description of the aharonov-bohm effect. *Phys. Rev. A* **106**, 032217 (2022).
22. Paiva, I. L., Dieguez, P. R., Angelo, R. M. & Cohen, E. Coherence and realism in the Aharonov-Bohm effect. *Phys. Rev. A* **107**, 032213 (2023).
23. Chang, M.-C. & Niu, Q. Berry phase, hyperorbits, and the hofstadter spectrum. *Phys. Rev. Lett.* **75**, 1348–1351 (1995).
24. Chang, M.-C. & Niu, Q. Berry phase, hyperorbits, and the hofstadter spectrum: semiclassical dynamics in magnetic bloch bands. *Phys. Rev. B* **53**, 7010 (1996).
25. Price, H. M., Zilberberg, O., Ozawa, T., Carusotto, I. & Goldman, N. Measurement of chern numbers through center-of-mass responses. *Phys. Rev. B* **93**, 245113 (2016).
26. Wimmer, M., Price, H. M., Carusotto, I. & Peschel, U. Experimental measurement of the berry curvature from anomalous transport. *Nat. Phys.* **13**, 545–550 (2017).
27. D'Errico, A. et al. Two-dimensional topological quantum walks in the momentum space of structured light. *Optica* **7**, 108–114 (2020).
28. Bernevig, B. A. *Topological Insulators and Topological Superconductors* (Princeton Univ. Press, 2013).
29. Asbóth, J. K. et al. *A Short Course on Topological Insulators* (Springer, 2016).
30. Duca, L. et al. An aharonov-bohm interferometer for determining bloch band topology. *Science* **347**, 288–292 (2015).
31. Provost, J. & Vallee, G. Riemannian structure on manifolds of quantum states. *Commun. Math. Phys.* **76**, 289–301 (1980).
32. Srivastava, A. & Imamoğlu, Amc Signatures of bloch-band geometry on excitons: nonhydrogenic spectra in transition-metal dichalcogenides. *Phys. Rev. Lett.* **115**, 166802 (2015).
33. Peotta, S. & Törmä, P. Superfluidity in topologically nontrivial flat bands. *Nat. Commun.* **6**, 8944 (2015).
34. Bleu, O., Malpuech, G., Gao, Y. & Solnyshkov, D. D. Effective theory of nonadiabatic quantum evolution based on the quantum geometric tensor. *Phys. Rev. Lett.* **121**, 020401 (2018).
35. Bleu, O., Solnyshkov, D. D. & Malpuech, G. Measuring the quantum geometric tensor in two-dimensional photonic and exciton-polariton systems. *Phys. Rev. B* **97**, 195422 (2018).
36. Gianfrate, A. et al. Measurement of the quantum geometric tensor and of the anomalous hall drift. *Nature* **578**, 381–385 (2020).
37. Törmä, P. Essay: where can quantum geometry lead us? *Phys. Rev. Lett.* **131**, 240001 (2023).
38. Su, W.-P., Schrieffer, J. & Heeger, A. Soliton excitations in polyacetylene. *Phys. Rev. B* **22**, 2099 (1980).
39. Castro Neto, A. H., Guinea, F., Peres, N. M. R., Novoselov, K. S. & Geim, A. K. The electronic properties of graphene. *Rev. Mod. Phys.* **81**, 109–162 (2009).
40. Cardano, F. et al. Detection of zak phases and topological invariants in a chiral quantum walk of twisted photons. *Nat. Commun.* **8**, 15516 (2017).
41. Maffei, M., Dauphin, A., Cardano, F., Lewenstein, M. & Massignan, P. Topological characterization of chiral models through their long time dynamics. *New J. Phys.* **20**, 013023 (2018).
42. D'Errico, A. et al. Bulk detection of time-dependent topological transitions in quenched chiral models. *Phys. Rev. Res.* **2**, 023119 (2020).
43. Bliokh, K. Y., Alonso, M. A. & Dennis, M. R. Geometric phases in 2d and 3d polarized fields: geometrical, dynamical, and topological aspects. *Rep. Prog. Phys.* **82**, 122401 (2019).
44. Meier, E. J. et al. Observation of the topological anderson insulator in disordered atomic wires. *Science* **362**, 929–933 (2018).
45. Haller, A., Massignan, P. & Rizzi, M. Detecting topology through dynamics in interacting fermionic wires. *Phys. Rev. Res.* **2**, 033200 (2020).
46. St-Jean, P. et al. Measuring topological invariants in a polaritonic analog of graphene. *Phys. Rev. Lett.* **126**, 127403 (2021).
47. D'Errico, A. et al. Bloch–Landau–Zener dynamics induced by a synthetic field in a photonic quantum walk. *APL Photonics* https://doi.org/10.1063/5.0037327 (2021).
48. Esposito, C. et al. Quantum walks of two correlated photons in a 2d synthetic lattice. *Npj Quantum Inf.* **8**, 34 (2022).
49. Di Colandrea, F. et al. Ultra-long quantum walks via spin–orbit photonics. *Optica* **10**, 324–331 (2023).

Acknowledgements

This work was supported by the Canada Research Chair (CRC) Program, NRC-uOttawa Joint Centre for Extreme Quantum Photonics (JCEP) via the Quantum Sensors Challenge Program at the National Research Council of Canada, and Quantum Enhanced Sensing and Imaging (QuEnSI) Alliance Consortia Quantum grant. FDC and FC acknowledge support from the PNRR MUR project PE0000023-NQSTI. We would also like to acknowledge one of the Reviewers who pointed out the relationship between the quantum metric and the quantity probed by the MCD.

Author contributions

A.D. conceived the idea and developed the theory. F.D.C., with contributions from N.D. and A.D., performed the simulations. F.D.C. and N.D. fabricated the plates and performed the experiment and data analysis. F.C. and E.K.

supervised the project. All authors contributed to the writing of the manuscript.

Competing interests
The authors declare no competing interests.

Additional information
Supplementary information The online version contains supplementary material available at https://doi.org/10.1038/s42005-024-01746-y.

Correspondence and requests for materials should be addressed to Alessio D'Errico.

Peer review information *Communications Physics* thanks Da-Wei Wang and the other, anonymous, reviewer(s) for their contribution to the peer review of this work. A peer review file is available.